energies

MDPI

Article

Thermal Performance Characteristics of a Microchannel Gas Heater for Solar Heating Applications

Bo Yang [1], Mohammad Mohsen Sarafraz [2,*] and Maziar Arjomandi [1]

[1] School of Mechanical Engineering, University of Adelaide, Adelaide, SA 5000, Australia; bo.yang01@adelaide.edu.au (B.Y.); maziar.arjomandi@adelaide.edu.au (M.A.)
[2] School of Engineering, Deakin University, Waurn Ponds, Geelong, VIC 3216, Australia
* Correspondence: mohsen.sarafraz@deakin.edu.au; Tel.: +61-41631-1335

Abstract: In the present article, the heat transfer and fluid flow of the air in a compact microchannel gas heater (MCGH) was experimentally quantified. To understand the effect of heat flux value (HFV), and inlet velocity on the heat transfer coefficient (HTC), wall temperature, friction factor, Nusselt number, average pressure-drop value (PDV) and performance index (PI), a microchannel gas heater was constructed and tested with pressurized air. The results showed that the HTC was 20 W/(sqmK) to 70 W/(sqmK), corresponding to inlet velocities 6.7 m/s and 16.7 m/s, respectively within HFV < 1 kW/m^2. Also, the highest PI was 1.19 meaning that the HT rate can be increased by 19% at u = 15 m/s in comparison with the reference case (at u = 13.3 m/s). Likewise, the HTC was intensified once the inlet velocity is increased. It was also identified that increasing the HFV has a strong effect on wall temperature, however, slightly changes the HTC. By increasing the heat flux value from 200 W/sqm to 1000 W/sqm, the HTC increased only by 4.7% which was associated with the poor thermophysical properties of air flowing inside MCGH. Two main mechanisms of wall slip and viscous heating were identified as main contributors to the heat transfer enhancement in MCGH.

Keywords: convective heat transfer; solar receiver; microchannel; thermal performance

Citation: Yang, B.; Sarafraz, M.M.; Arjomandi, M. Thermal Performance Characteristics of a Microchannel Gas Heater for Solar Heating Applications. *Energies* **2021**, *14*, 7625. https://doi.org/10.3390/en14227625

Academic Editor: Gabriela Huminic

Received: 28 October 2021
Accepted: 11 November 2021
Published: 15 November 2021

1. Introduction

Solar energy is an abundant and available renewable resource that can be integrated into process heats to decrease the emission of greenhouse gases and promote the fuel economy of the energy systems. Concentrated Solar Tower Technology (CSTT) is one of the most efficient solar energy technologies which provides high solar-to-electric conversion efficiency and large-scale continuous generation of solar electricity [1]. By utilising heliostats, the CSTT concentrates the reflected solar radiation to a solar receiver on the top of the solar tower. Consequently, the solar power is transferred into the heat in the working fluid such as molten salt, oil, steam and air, which drives turbines to generate electricity. Recently, several concentrated solar tower systems equipped with molten salt receivers and steam receivers have been commercially operated worldwide [2–5]. While molten salt is a promising heat transfer fluid, corrosion and technical challenges associated with storage, pumping, and handling molten salts are barriers and limitations that require further research and development.

Solar air receiver is an emerging technology that uses air as the working fluid to absorb heat from solar energy and transfer it to any integrated process. The utilisation of air as heat transfer fluid can potentially eliminate pipe clogging and temperature limitation of conventional receivers while addressing technical challenges associated with molten salts. Since the conceptual design was demonstrated by Jarvinen et al. [6], various configurations of air receivers were investigated by different researchers to identify the bottlenecks and a plausible configuration with the potential to enhance the technology readiness level. For example, Qiu et al. [7] studied the thermal characteristics of a helically coiled tube cavity receiver. They used pressurised air inside a coiled tube with an inner diameter

of 12 mm at the flow rate of 1~5 m^3/h under an average heat flux value (HFV) up to 300 kW/sqm. Their results indicated that with the decrease in the inner radius of the coiled tube, both the thermal efficiency and the pressure drop value (PDV) increased. Pabst et al. [1] investigated the performance of a metallic air receiver with a cellular honeycomb structure. They used corrugated and flat metal foils to form the air channels with increased local turbulence and radial flow. The constructed receiver provided a high efficiency of 80% when the outlet temperature was >800 °C. Roldan et al. [8,9] designed and tested a ceramic-made air receiver embedded with a porous material. They showed that porosity is the controlling parameter for the thermal efficiency of the air receiver and even solar flux distribution is the key for obtaining high thermal efficiency. There are extensive studies conducted on various configuration of air receives including quartz tube receiver, ceramic foam volumetric receiver and wire mesh receiver reported by various researchers [10–12].

A microchannel gas heater (MCGH) is an emerging technology that can provide a high heat transfer coefficient (HTC) under a laminar flow regime together with high energy efficiency, reliability, and scalability. Since the pioneering work of Tuckerman and Pease [13], there has been a growing interest in the application of microchannels over the few decades [14–22]. As one of the highly efficient heat exchangers, a microchannel can also be used as a solar receiver. Recently, Ahlatli et al. [23] conducted a series of experiments to analyse the heat transfer (HT) characteristics of carbon nanotube-water nanofluid inside a microchannel solar receiver. Their study revealed that using a microchannel as a solar receiver with nanofluids can achieve a plausible thermal performance (TP).

Several studies also reported the applications of microchannel receivers using other working fluids such as water and two-phase flows such as air-water systems [24–26]. Despite the successful demonstration of microchannel for heating/cooling applications of nanofluids, however, the performance of microchannel solar air receivers has been rarely investigated. Li et al. [27] designed and tested a mini-channel solar air receiver with 1 mm width channels and 2 mm high ribs. The air inlet pressure of up to 6 bar and the mass flow rate of up to 0.8 g/s under the solar HFV of 170–470 kW/sqm was tested inside the air receiver. They found that the HTC can be enhanced by increasing the airflow rate and also the HFV. In another research, Menni et al. [28] studied the heat transfer performance of hydrogen gas in a baffled compact heat exchanger and showed that for 5000 < Re < 25,000, the heat transfer performance can be as high as 1.25 which was suitable for automotive, and chemical industries. In further research, they improved the design of the compact heat exchanger by changing geometrical specification and hydraulic space of the heat exchanger [28,29].

To understand the mechanism of HT inside a microchannel, Zhu et al. [30] studied the convective HT of a laminar gas flowing inside a microchannel in the slip flow regime. The effects of channel aspect ratio, Knudsen number and thermal boundary conditions on the HT process inside the microchannel were theoretically analysed. It was identified that due to the thermal resistance caused by the wall slip effect, the HTC decreased, which was further confirmed by other studies on the wall slip effect in microchannel [31–34]. Meanwhile, the viscous dissipation effect also influences the thermal efficiency of fluid and gas, which was analytically and experimentally investigated in literature [35–38].

In light of the above literature, a microchannel has the potential to be utilised as the solar air receiver to harness solar energy effectively. Air as a working fluid can be a solution to technical challenges associated with molten salts, however, there is a shortcoming in understanding the behaviour of air inside a microchannel heat exchanger. Accordingly, in the present work, a series of experiments are conducted aiming at quantifying the TP of a microchannel solar air receiver at various operating conditions. The HTC, PDV and the TP of the system are measured for a copper-made microchannel air gas heater with channel dimensions of "0.2 mm × 0.2 mm", "0.4 mm × 0.2 mm", and "0.2 mm × 0.4 mm" under 0.2–1 kW/sqm to be in synergy with solar HFV. The influence of applied HFV, air velocity, channel aspect ratio, wall slip and viscous heating effect on the TP of the receiver is experimentally investigated and discussed. The experimental data are correlated against

non-dimensional parameters to develop equations that can predict Nusselt number for air inside the microchannel.

2. Experimental Section

2.1. Experimental Setup

As illustrated in Figure 1, the process diagram of the constructed rig for measuring the TP of the air gas heater used in this study. The rig consists of the following main components:

(1) A microchannel solar air receiver test section including 250 rectangular alike channels with the same aspect ratio and thickness attached to a silicone film heater and the microchannel block;
(2) An air piping system including air hose, a pressure regulator, valves and fittings;
(3) Instruments and data recording system including a flow meter (manufactured by Key Instruments, accuracy: ±4% of full scale), five thermocouples (type k), two pressure measurement transmitters (manufactured by DCBox, accuracy: ±0.5% with line for connecting to a data logger) and a system for logging the real time data (manufactured by Pico).

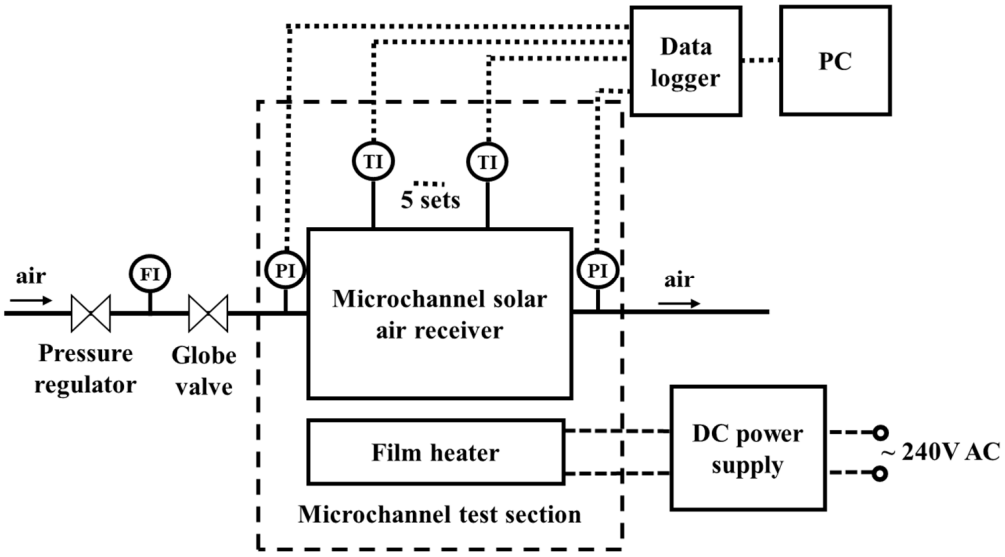

Figure 1. Flow diagram of the MCGS solar air receiver. (TT: Temperature Transmitter; PT: Pressure Transmitter; FI: Flow rate Indicator).

The pressurised air was sourced from the Mechanical Engineering building at the University of Adelaide with the capacity of supplying a large flow rate of air at various pressures up to 10 bar. The inlet air pressure was maintained by a manual pressure regulator equipped with a manometer and a gauge. The volumetric flow rate, temperature and pressure at the entry and exit ports were measured using a flow meter and thermocouples (category k) and two pressure point transmitters (PPT), respectively (collectively shown on Figures 1 and 2). Likewise, three thermocouples were installed at the top of the microchannel test section to record the channel surface temperature at the axial positions of z = 0, 25, 50, 75 and 100 mm, respectively (z = 0 at the entry region). Silicon HT compound was applied to the thermo-wells to fill any gaps and to suppress any potential contact resistance between the tip of the thermocouples and the walls of the microchannel. A data logger system (manufactured by Pico Co., UK) was used to collect the data of temperatures and pressures from the instruments. Detailed information on the constructed test rig is depicted in Figure 2. The film heater was attached to the bottom of the microchannel to provide thermal energy required for heating the air, which was controlled by a laboratory power source (12/24 V DC GW Instek). The constructed MCGH was created using CNC

machining from the computer-aided design (CAD) files. Figure 3 shows the microscopic images taken from the microchannel created on the copper block at various aspect ratios.

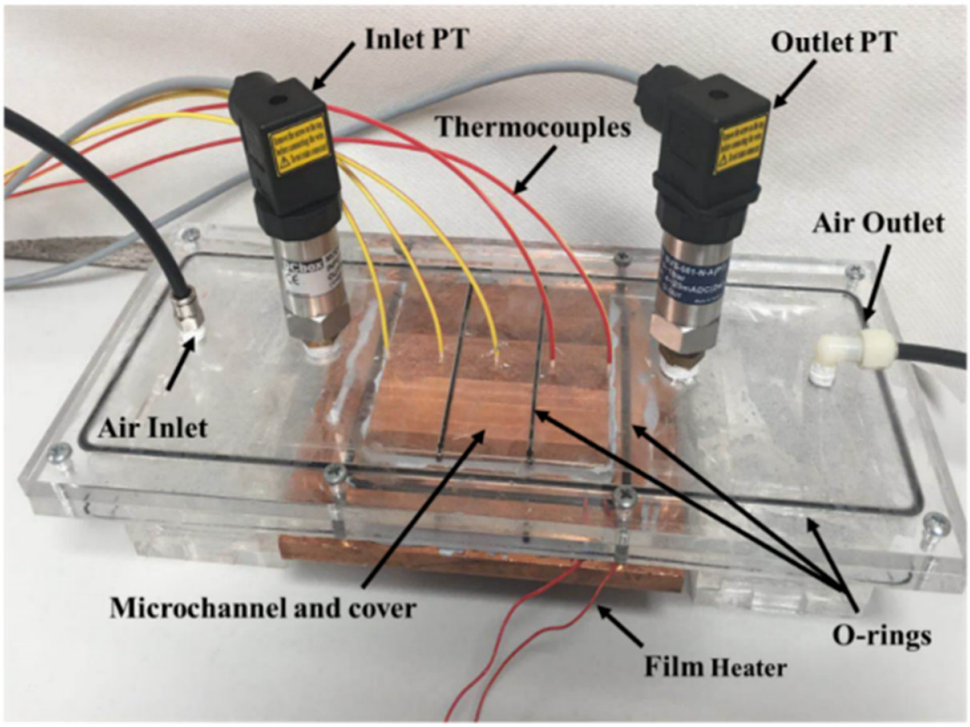

Figure 2. Microchannel solar air receiver test rig equipped with instruments.

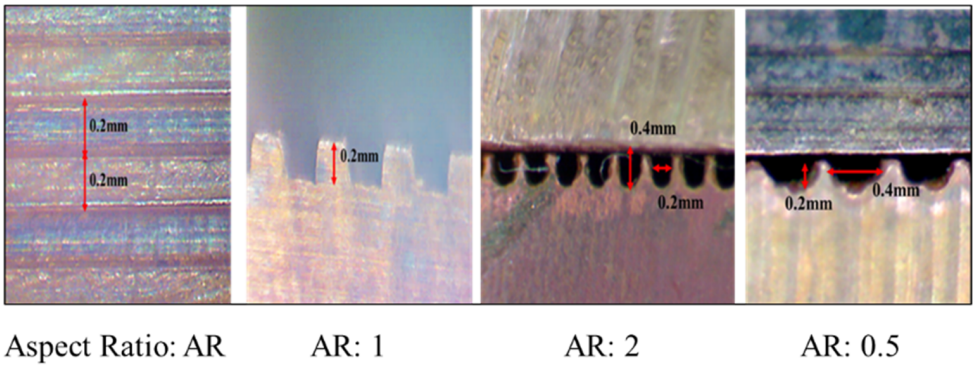

Figure 3. The constructed microchannel at various aspect ratios was used in the present research.

2.2. Test Rig Reliability and Data Validation

Figure 4 shows the variation of the calculated friction factor and those recorded experimentally with Reynolds number at various inlet velocities. As can be observed, the calculated friction factor values stand within ±4.1% deviation against data measured experimentally. Also, the measured data followed the Darcy trend showing that the measurements are aligned with theoretical calculations. Likewise, the calculated outlet temperature from the microchannel gas heater was compared to those experimentally measured during the validation stage. As shown, the measured outlet temperatures are in good agreement within ±5% against experimental data as shown in Figure 5. Accordingly, the test rig has sufficient fidelity for HT study and flow measurements.

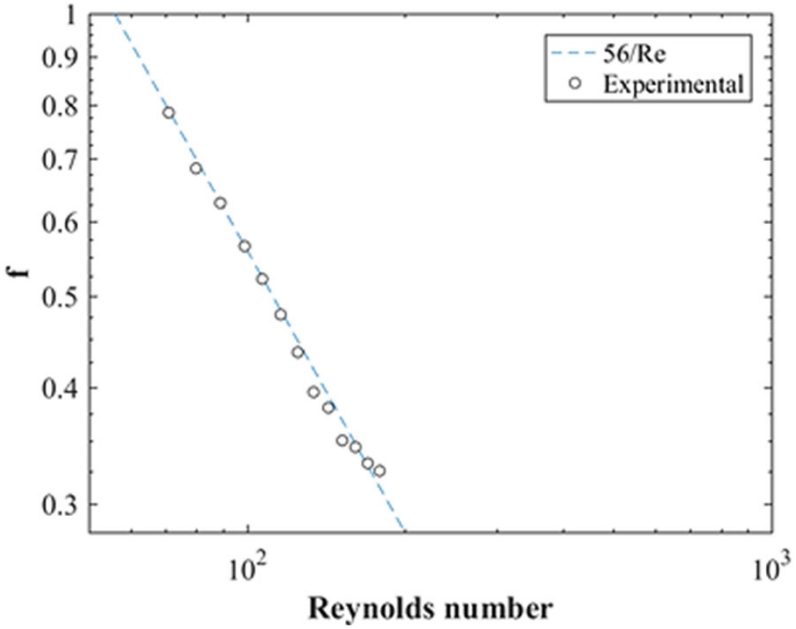

Figure 4. The comparison of the theoretical and experimental friction factor values at different Reynolds numbers.

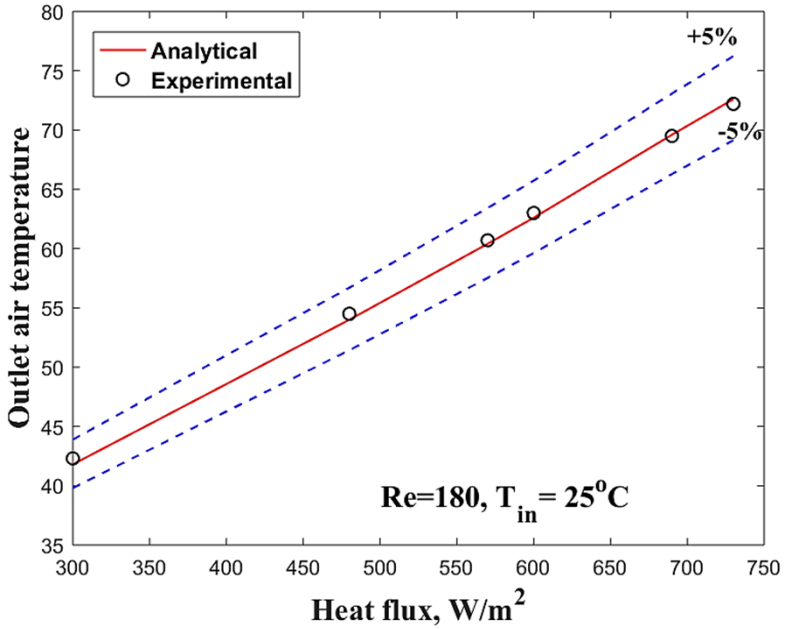

Figure 5. The comparison between the analytically calculated outlet air temperature and the experimental results at different heat fluxes.

2.3. Uncertainty Analysis

Based on the values expressed in Table 1, an uncertainty analysis was conducted aiming at identifying the reliability of the experimental data and the accuracy of the data interpretation. To calculate the errors, the uncertainty technique developed by Moffat et al. [39] was utilised according to the following equation:

$$\frac{\delta R}{R} = \left\{ \left(a\frac{\delta x_1}{x_1} \right)^2 + \left(b\frac{\delta x_2}{x_2} \right)^2 + \cdots + \left(N\frac{\delta x_n}{x_n} \right)^2 \right\}, \; R = {x_1}^a {x_2}^b \cdots {x_n}^N \tag{1}$$

Table 1. The calculated and/or claimed-by-manufacturer accuracy of the instruments.

Parameters	Range	Instrument	Uncertainty
Temperature (°C)	30–70	K-type thermocouple	±0.5 °C
Heater throughput (W)	0–180	DC Power	±0.5%
Flow rate (L/min)	1–10	KI MR series	±4%
Pressure (Bar)	0–1	BVS series	±0.5%
Air velocity (m/s)	<20	-	±4%
Re	100–180	-	6.8%
Pr	-	-	5%
HTC	-	-	8.5%
f	-	-	6%

2.4. Calculation of Thermal Performance

The HT between the air and the microchannel wall was calculated using the following equation:

$$Q = \dot{m}_a \cdot C_a (T_o - T_i) \tag{2}$$

Here, Q is the amount of heat that is exchanged between MCGH and air; $\dot{m}_a$ and C_a are the mass flow rate and the specific heat of air, respectively. T_o and T_i are temperatures at the entry and exit ports of the MCGH. $Q''_{conv.}$ is the convective HT flux that is calculated by:

$$Q''_{conv.} = \frac{Q}{A} \tag{3}$$

The convective HTC can be calculated by the following equation:

$$h = \frac{Q''_{conv.}}{T_w - T_a} \tag{4}$$

where T_w and T_a are the wall temperature and air temperature, respectively. The Reynolds number is calculated using Equation (5):

$$\mathrm{Re} = \frac{\rho_a u_a D_h}{\mu_a} \tag{5}$$

Here, ρ_a, μ_a and u_a are the density, viscosity and the average velocity of the air inside the microchannel, respectively; D_h is the hydraulic diameter of the microchannel. The friction factor (f) can be obtained using Equation (6):

$$f = \frac{\Delta P_a}{\frac{l}{D_h} \cdot \frac{\rho_a {u_a}^2}{2}} \tag{6}$$

The equations for the calculation of the air physical properties were collected and expressed in Table 2.

Table 2. Equations for calculating the physical properties of air [40].

Parameter	Value	Range (K)	Unit
$C_{p,a}$	$\left(A + B \cdot \left(\frac{C/T}{\sinh(C/T)}\right)^2 + D \cdot \left(\frac{E/T}{\cosh(E/T)}\right)^2\right) \cdot \frac{1}{28.966}$ A = 2.8 E4, B = 9.3 E3, C = 3 E3, D = 7.5 E2, E = 11.48 E2	$50 \le T \le 1500$	J/(kg·K)
μ_a	$\frac{A \cdot T^B}{1 + C/T}$ A = 1.425×10^{-6}, B = 0.5039, C = 108.3	$80 \le T \le 2000$	kg/(m·s)
k_a	$\frac{A \cdot T^B}{1 + C/T + D/T^2}$ A = 0.00031417, B = 0.7305, C = −18.63, D = 440	$30 \le T \le 2000$	W/(m·K)

3. Results and Discussion

3.1. Wall Temperature across the Microchannel

Figure 6 depicts the variation of the wall temperature with distance from the inlet (position of the thermocouples) at a constant HFV of 300 W/sqm and for an inlet air

temperature of 25 °C at various air velocities. As shown, two domains can be identified: In domain I, the wall temperature suddenly increases at the inlet region and then linearly ramps up reaching the second domain. In domain II, the wall temperature slightly changes with distance from the entry of the MCGH and it remains unchanged at the region close to the outlet of the microchannel. For example, at u = 6.7 m/s, the wall temperature increases from 36.2 °C to 72.2 °C at 0~0.025 m (domain I), whereas the wall temperature increases linearly from 72.2 °C to 74.2 °C at 0.025~0.1 m (domain II). Moreover, the wall temperature decreases with the increase in the air velocity. For example, the wall temperature at the outlet is 74.2 °C at u = 6.7 m/s, but it decreases to 43.0 °C at u = 16.7 m/s. This is associated with the enhancement in the HTC which in turn increases the HT rate from walls to the air. Consequently, lower wall temperature was recorded at higher air velocity values. The inlet of the microchannel is located on the left side of each figure.

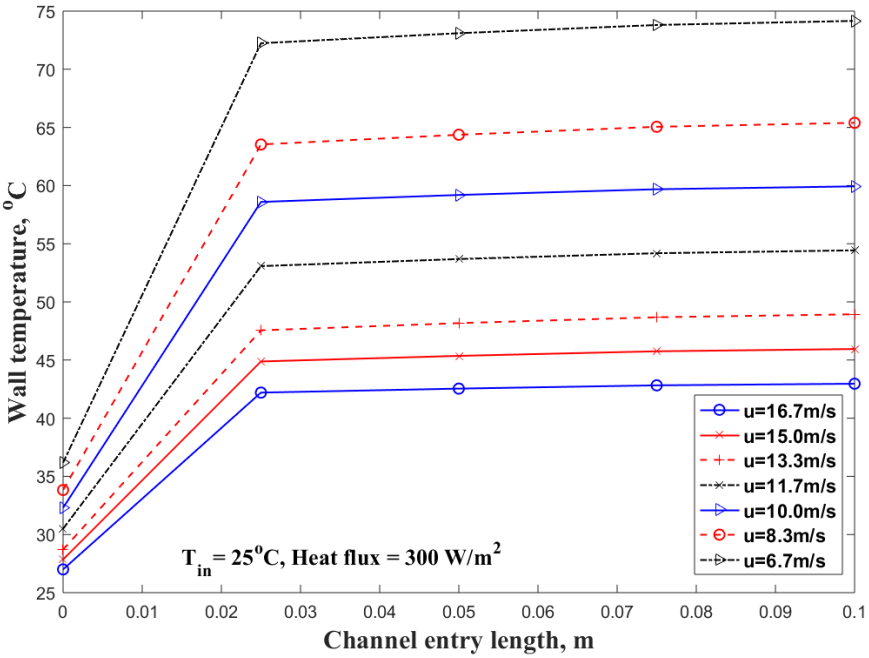

Figure 6. Effect of distance from the inlet on linear wall temperature profile at T = 25 °C and HFV of 300 W/sqm.

Figure 7 shows the microchannel wall temperature distribution in the axial direction at a constant air velocity of 16.7 m/s and an inlet air temperature of 25 °C, at various heat fluxes ranging from 300 W/sqm to 800 W/sqm. Interestingly, the same trend is identified such that with an increase in the power throughput of the heater (HFV), the wall temperature increases. For example, at an HFV of 300 W/sqm, the wall temperature increases from 27.0 °C to 42.2 °C at 0~0.025 m, then it increases linearly from 42.2 °C to 43.0 °C at 0.025~0.1 m; however, at an HFV of 800 W/sqm, the wall temperature at 0, 0.025 m and 0.1 m location is 37.5 °C, 74.6 °C and 77.3 °C respectively.

3.2. Wall Temperature across the Microchannel

Figure 8 shows the variation of the HTC with the applied HFV to the microchannel with a channel dimension of 0.2 mm × 0.2 mm for air at various velocities. The HTC value slightly increases with the increase in the HFV value. For example, at a velocity of 16.7 m/s, the HTC at an HFV of 200 W/sqm is 59.4 W/sqmK, while for HFV of 800 W/sqm, the HTC increases to 65.9 W/sqmK. Likewise, increasing the air velocity further intensifies the HTC value. For example, at a HFV of 800 W/sqm, the HTC value at u = 6.7 m/s is 26.2 W/sqmK, while at u = 15.0 m/s, the HTC = 60.4 W/sqmK. The highest HTC of 66.4 W/sqmK was recorded at an HFV of 1100 W/sqm and u = 16.7 m/s.

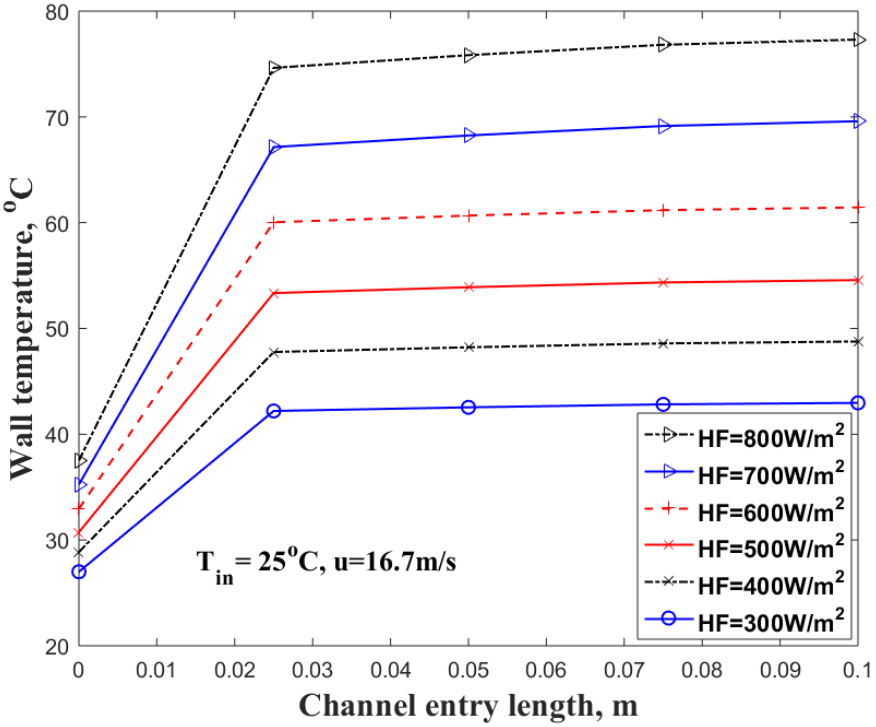

Figure 7. Effect of distance from the inlet on linear wall temperature profile at T = 25 °C and u = 16.7 m/s.

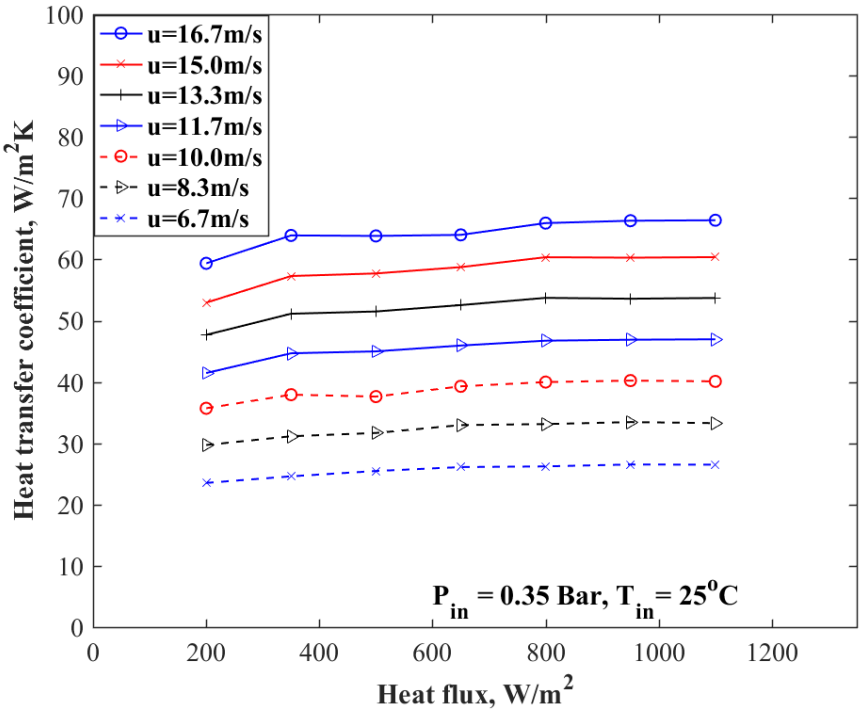

Figure 8. The effect of heater throughput (HFV) on the convective HTC at T= 25 °C.

Figure 9 shows the corresponding Nusselt numbers associated with HTC values reported in Figure 8. As shown, the variation of the Nusselt number with the applied HFV shows that the higher Nu can be achieved with an increase in the flow rate and the applied HFV.

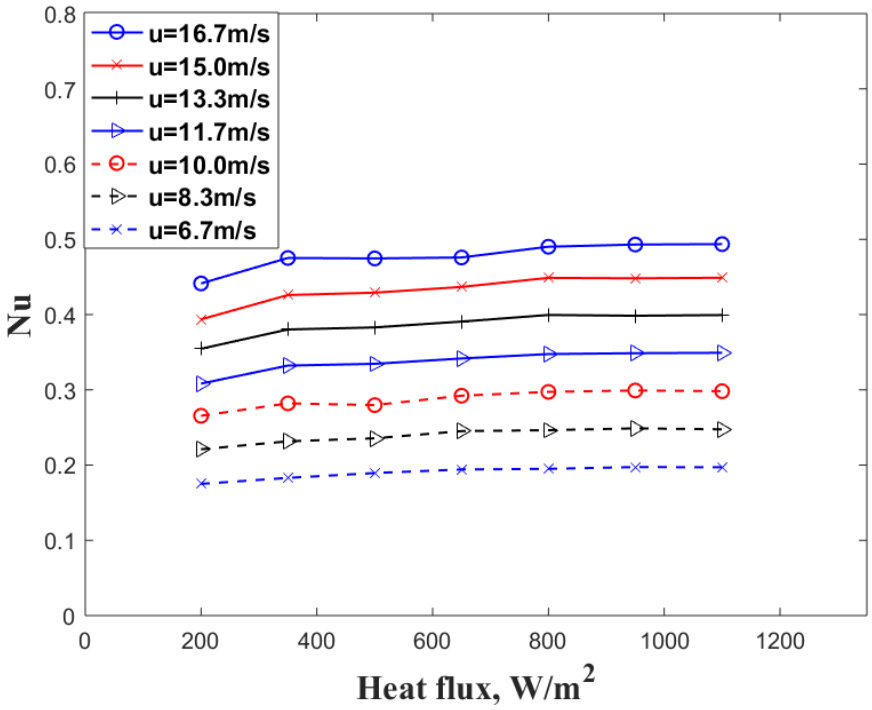

Figure 9. The variation of the Nusselt number with the HFV at various volume flow rates of air and inlet temperature of 25 °C.

3.3. Pressure-Drop across the Microchannel

Figure 10 depicts the variation of the PDV with Reynolds number for a microchannel with a channel dimension of 0.2 mm × 0.2 mm. As shown, with increasing the Reynolds number, a relatively linear increase in PDV is observed. For example, at Re = 107, the measured PDV is 14.8 kPa, but for Re = 170, the PDV increases to 28.5 kPa. Notably, the experimental data for the PDV is in agreement with the ones in the following literature [19,20,41,42].

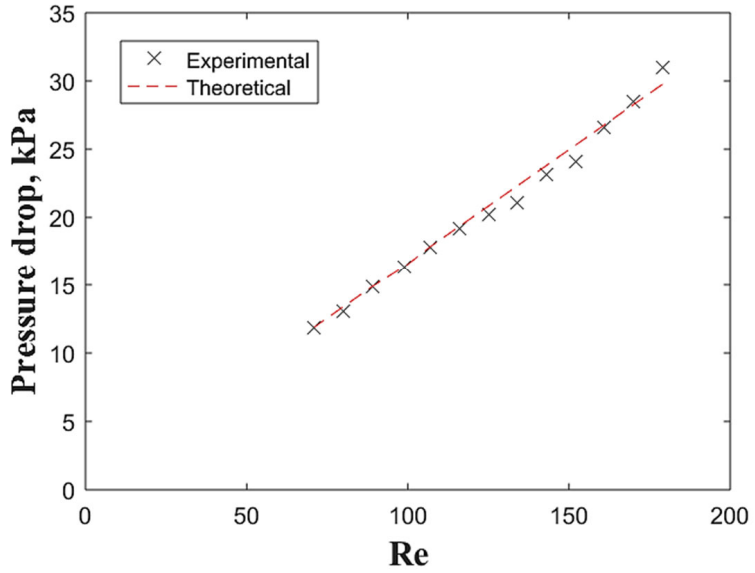

Figure 10. The variation of the PDV of the microchannel with Reynolds number for microchannel with a channel dimension of 0.2 mm × 0.2 mm.

3.4. The Aspect Ratio of the Microchannel

Figure 11 shows the calculated Nusselt numbers for microchannel with different channel dimensions at different Reynolds numbers. As can be seen, the aspect ratio (AR), can affect the Nusselt number. As shown, the best TP is observed at AR = 1 in which the Nusselt number reaches its largest value. For example, for a given Re = 10, at AR = 1, the Nu = 0.55, while at AR = 0.1 and AR = 2, the Nusselt number is 0.42 and 0.34, respectively. Accordingly, for air, the aspect ratio of 1: 1 is suggested to be utilised when designing a microchannel gas heater in which the Nusselt number is 30% higher than AR = 0.5 and 61.7% higher than AR = 2.

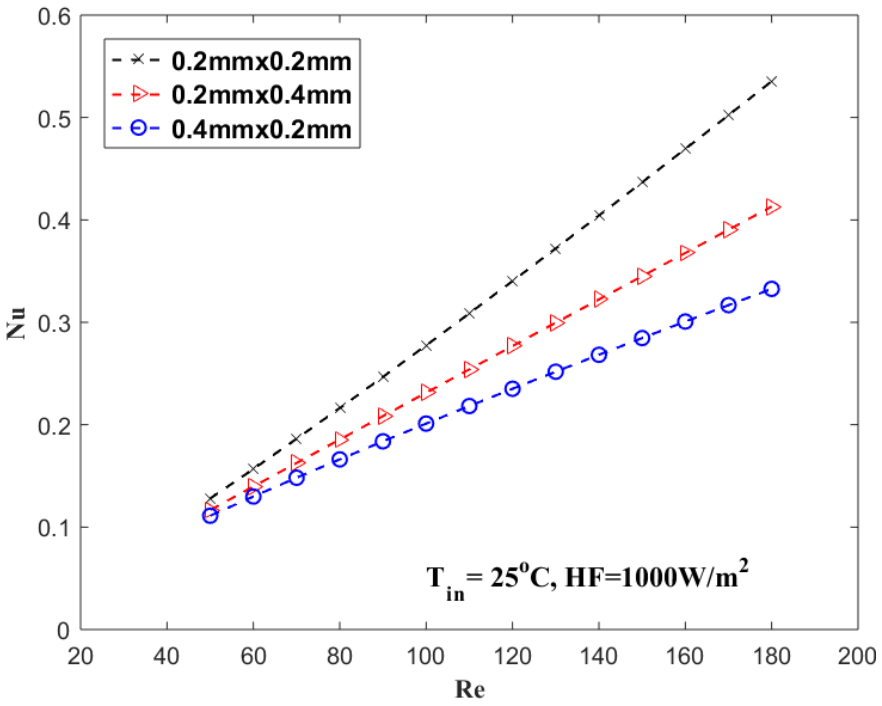

Figure 11. The calculated Nusselt number at various Reynolds numbers.

3.5. Thermal Performance

Due to the trade-off trend between HTC and the PDV observed in the measurements, the TP of the compact gas heater cannot be calculated merely based on the Nusselt number. Accordingly, Equation (7) was utilised to account for the PDV associated with the increase in the flow rate of the air. This equation identifies the optimum condition for the MCGH in which the PDV is low, while the HTC value is the highest:

$$P.I. = \frac{\mathrm{Nu}}{\mathrm{Nu}_{ref}} \times \left(\frac{f_{ref}}{f}\right)^{\frac{1}{3}} \tag{7}$$

In this equation, Nu is the Nusselt number, and ΔP is the PDV of the fluid in the microchannel. According to Figure 12, the variation of P.I with various air velocities shows that the best performance index can be obtained at an inlet velocity of 15 m/s in which despite the high-PDV, the increase in the Nusselt number can compensate for the augmentation of the friction forces due to the increase in the velocity of air. However, for other velocities, the performance index is smaller than 1 which means that the penalty and loss associated with augmented PDV are higher than the gain that can be obtained from the enhancement of the Nusselt number.

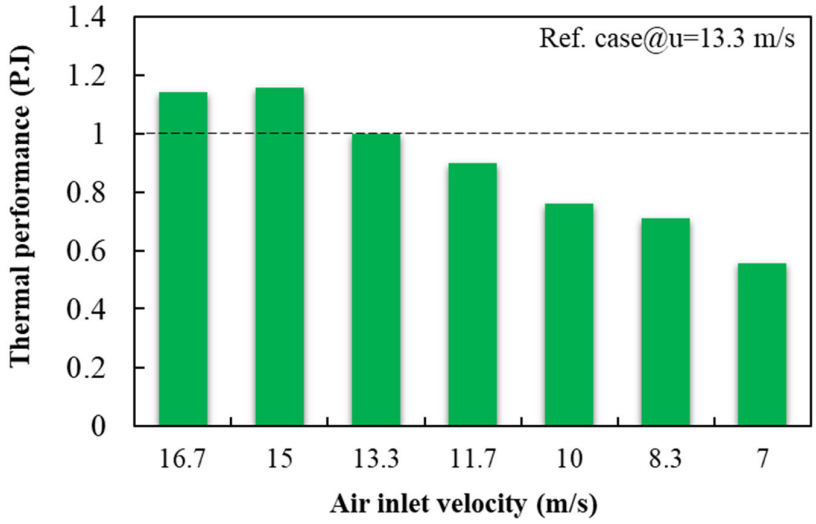

Figure 12. Effect of air inlet velocity on the calculated thermal performance index (PI).

4. Mechanism of Heat Transfer

Wall slip effect and viscous heating are two major contributors to the convective HT from microchannel to the air which is discussed in this section:

Wall slip effect: By comparing the values of HTC value and Nu, it can be stated that the measured value in this work is relatively lower than those calculated by the theoretical values for rectangular channels under non-slip conditions. However, these low values are justifiable when the wall slip effect is taken into the consideration and the magnitude of the Nu number is in good agreement with the data extracted from the literature in which the "wall slip effect" was considered as the main contributor to HT [30,32–34,43–51].

Viscous heating: Due to the viscous heating effect, the HTC value of air slightly increases with the increase of applied HFV, which is similar to the data found in the literature [19,21,35,36,38,52–55]. The Brinkman number, which is the ratio between heat produced by viscous dissipation and the heat transferred by conduction, was used to describe the impact of viscous dissipation on HT in small channels or pipes:

$$Br = \frac{\mu u^2}{D_h q''} \tag{8}$$

With increasing the HFV, the Brinkman number is suppressed, thereby reducing the viscous heating effect. Hence, the HTC value increases.

5. Conclusions

To evaluate the performance of the microchannel gas heater, a series of experiments were designed and conducted to investigate the values of HTC, PDV, at various operating conditions. Air was utilised as a heat transfer fluid under laminar regime and MCGH was operated at low HFV up to 1 kW/m^2 to be in synergy with solar flux. The following conclusions were drawn:

- The validation of the system against (56/Re) equation showed that the air flow followed the Darcy equation. Validation of the outlet temperature of the system showed that both HT and fluid flow characteristics were in a good agreement within ±5% deviation. Likewise, the Darcy equation showed sufficient accuracy to be used for describing the relationship between the friction factor, PDV and fluid flow rate inside the microchannel.
- The quantified HTC values were intensified by increasing the inlet velocity of the air and also increased by increasing the power throughput of the heater.

- The wall temperature profile represented two distinguished domains. In domain I near the entry region of the microchannel, the temperature quickly increased reaching its 98% value, while in domain II, the temperature gradually ramped up.
- The aspect ratio, AR = 1 was identified as the best geometrical specification for the test microchannel in which the Nusselt value was the highest. Also, wall slip and viscous heating effects were two main contributors to the HT that justified the trends observed in the experiments.

Overall, the microchannel solar air receiver showed a plausible potential at low HFV (e.g., 1 kW/sqm) for heating gases. However, further experiments with other gases and geometrical specifications are required to advance the knowledge in understanding the mechanism of HT and optimum design of microchannel gas heaters for solar applications.

Author Contributions: Conceptualization, B.Y., M.M.S., M.A.; B.Y., M.A., M.M.S.; validation, B.Y.; formal analysis B.Y.; investigation, B.Y., M.A., M.M.S.; data curation, B.Y., M.M.S., M.A.; writing—original draft preparation, B.Y.; writing—review and editing, M.A., M.M.S.; supervision, M.A. All authors have read and agreed to the published version of the manuscript.

Funding: This research received no external funding.

Institutional Review Board Statement: Not applicable.

Informed Consent Statement: Not applicable.

Data Availability Statement: All available data has already been provided in the manuscript.

Acknowledgments: Mohammad Mohsen Sarafraz gratefully acknowledge the "Vice-chancellor Alfred Deakin Postdoctoral Research Fellowship" program. All authors acknowledge the financial support and facilities shared by School of Engineering, the University of Adelaide.

Conflicts of Interest: The authors declare no conflict of interest.

References

1. Pabst, C.; Feckler, G.; Schmitz, S.; Smirnova, O.; Capuano, R.; Hirth, P.; Fend, T. Experimental performance of an advanced metal volumetric air receiver for Solar Towers. *Renew. Energy* **2017**, *106*, 91–98. [CrossRef]
2. Dunn, R.I.; Hearps, P.J.; Wright, M.N. Molten-Salt Power Towers: Newly Commercial Concentrating Solar Storage. *Proc. IEEE* **2012**, *100*, 504–515. [CrossRef]
3. Avila-Marin, A.L.; Fernandez-Reche, J.; Tellez, F.M. Evaluation of the potential of central receiver solar power plants: Configuration, optimization and trends. *Appl. Energy* **2013**, *112*, 274–288. [CrossRef]
4. Overton, T.W. Ivanpah solar electric generating system earns Power's highest honor.(Plant of the Year)(Cover story). *Power* **2014**, *158*, 26.
5. Py, X.; Azoumah, Y.; Olives, R. Concentrated solar power: Current technologies, major innovative issues and applicability to West African countries. *Renew. Sustain. Energy Rev.* **2013**, *18*, 306–315. [CrossRef]
6. Jarvinen, P.O. Solar-heated-air receivers. *Sol. Energy* **1977**, *19*, 139–147. [CrossRef]
7. Qiu, K.; Yan, L.; Ni, M.; Wang, C.; Xiao, G.; Luo, Z.; Cen, K. Simulation and experimental study of an air tube-cavity solar receiver. *Energy Convers. Manag.* **2015**, *103*, 847–858. [CrossRef]
8. Roldán, M.I.; Zarza, E.; Casas, J.L. Modelling and testing of a solar-receiver system applied to high-temperature processes. *Renew. Energy* **2015**, *76*, 608–618. [CrossRef]
9. Roldán, M.I.; Smirnova, O.; Fend, T.; Casas, J.L.; Zarza, E. Thermal analysis and design of a volumetric solar absorber depending on the porosity. *Renew. Energy* **2014**, *62*, 116–128. [CrossRef]
10. Wang, F.; Bai, F.; Wang, T.; Li, Q.; Wang, Z. Experimental study of a single quartz tube solid particle air receiver. *Sol. Energy* **2016**, *123*, 185–205. [CrossRef]
11. Wu, Z.; Wang, Z. Fully coupled transient modeling of ceramic foam volumetric solar air receiver. *Sol. Energy* **2013**, *89*, 122. [CrossRef]
12. Wu, Z.; Caliot, C.; Flamant, G.; Wang, Z. Coupled radiation and flow modeling in ceramic foam volumetric solar air receivers. *Sol. Energy* **2011**, *85*, 2374–2385. [CrossRef]
13. Tuckerman, D.B.; Pease, R.F. *Microcapiliary Thermal Interface Technology for VLSI Packaging*; IEEE: Piscataway, NJ, USA, 1983; pp. 60–61.
14. Azizi, Z.; Alamdari, A.; Malayeri, M.R. Convective heat transfer of Cu–water nanofluid in a cylindrical microchannel heat sink. *Energy Convers. Manag.* **2015**, *101*, 515–524. [CrossRef]
15. Ganji, D.D.; Malvandi, A. *Heat Transfer Enhancement Using Nanofluid Flow in Microchannels: Simulation of Heat and Mass Transfer*; William Andrew: New York, NY, USA, 2016.

16. Sehwan, I.; Baek, S.; Jin, L.; Jeong, S. Flow boiling heat transfer of R123/R134a mixture in a microchannel. *Exp. Therm. Fluid Sci.* **2018**, *99*, 474–486. [CrossRef]
17. Lee, P.S.; Chou, S.K.; Lee, Y.J. *Optimization of the Thermal Performance of Microchannel Heat Sinks Using Thermally Developing Nusselt Number Correlation*; IEEE: Piscataway, NJ, USA, 2008; pp. 545–551.
18. Li, D.-Y.; Li, X.-B.; Zhang, H.-N.; Li, F.-C.; Qian, S.; Joo, S. Efficient heat transfer enhancement by elastic turbulence with polymer solution in a curved microchannel. *Microfluid. Nanofluidics* **2017**, *21*, 1–13. [CrossRef]
19. Sarafraz, M.M.; Arjomandi, M. Thermal performance analysis of a microchannel heat sink cooling with copper oxide-indium (CuO/In) nano-suspensions at high-temperatures. *Appl. Therm. Eng.* **2018**, *137*, 700–709. [CrossRef]
20. Sarafraz, M.M.; Arya, H.; Arjomandi, M. Thermal and hydraulic analysis of a rectangular microchannel with gallium-copper oxide nano-suspension. *J. Mol. Liq.* **2018**, *263*, 382–389. [CrossRef]
21. Sarafraz, M.M.; Hart, J.; Shrestha, E.; Arya, H.; Arjomandi, M. *Experimental Thermal Energy Assessment of a Liquid Metal Eutectic in a Microchannel Heat Exchanger Equipped with a (10 Hz/50 Hz) Resonator*; Applied Thermal Engineering; Elsevier: Amsterdam, The Netherlands, 2019; Volume 148.
22. Yu, W.; Desmulliez, M.P.Y.; Drufke, A.; Leonard, M.; Dhariwal, R.S.; Flynn, D.; Bognár, G.; Poppe, A.; Horvath, G.; Kohari, Z.; et al. High-aspect-ratio metal microchannel plates for microelectronic cooling applications. *J. Micromech. Microeng.* **2010**, *20*, 025004. [CrossRef]
23. Ahlatli, S.; Maré, T.; Estellé, P.; Doner, N. Thermal performance of carbon nanotube nanofluids in solar microchannel collectors: An experimental study. *Int. J. Technol.* **2016**, *2*, 78–85. [CrossRef]
24. Ramos-Alvarado, B.; Li, P.; Liu, H.; Hernandez-Guerrero, A. CFD Study of Liquid-cooled Heat Sinks with Microchannel Flow Field Configurations for Electronics, Fuel Cells, and Concentrated Solar Cells. *Appl. Therm. Eng.* **2011**, *31*, 2494–2507. [CrossRef]
25. Rahimi, M.; Karimi, E.; Asadi, M.; Valeh-E-Sheyda, P. Heat transfer augmentation in a hybrid microchannel solar cell. *Int. Commun. Heat Mass Transf.* **2013**, *43*, 131. [CrossRef]
26. Valeh-E-Sheyda, P.; Rahimi, M.; Karimi, E.; Asadi, M. Application of two-phase flow for cooling of hybrid microchannel PV cells: A comparative study. *Energy Convers. Manag.* **2013**, *69*, 122. [CrossRef]
27. Li, Q.; Tourville, N.G.d.; Yadroitsev, I.; Yuan, X.; Flamant, G. Micro-channel pressurized-air solar receiver based on compact heat exchanger concept. *Sol. Energy* **2013**, *91*, 186–195. [CrossRef]
28. Menni, Y.; Ghazvini, M.; Ameur, H.; Kim, M.; Ahmadi, M.H.; Sharifpur, M. Combination of baffling technique and high-thermal conductivity fluids to enhance the overall performances of solar channels. *Eng. Comput.* **2020**, 1–22. [CrossRef]
29. Menni, Y.; Ghazvini, M.; Ameur, H.; Ahmadi, M.H.; Sharifpur, M.; Sadeghzadeh, M. Numerical calculations of the thermal-aerodynamic characteristics in a solar duct with multiple V-baffles. *Eng. Appl. Comput. Fluid Mech.* **2020**, *14*, 1173–1197. [CrossRef]
30. Zhu, X.; Liao, Q. Heat transfer for laminar slip flow in a microchannel of arbitrary cross section with complex thermal boundary conditions. *Appl. Therm. Eng.* **2006**, *26*, 1246–1256. [CrossRef]
31. Beskok, A.; Karniadakis, G.E.; Trimmer, W. Rarefaction and compressibility effects in gas microflows. *J. Fluids Eng.* **1996**, *118*, 448. [CrossRef]
32. Arkilic, E.B.; Schmidt, M.A.; Breuer, K.S. Gaseous slip flow in long microchannels. *J. Microelectromech. Syst.* **1997**, *6*, 167–178. [CrossRef]
33. Sparrow, E.M.; Lin, S.H. Laminar heat transfer in tubes under SLIP-flow conditions. *J. Heat Transf.* **1962**, *84*, 363–369. [CrossRef]
34. Mashhadi, M.R.; Croizet, C.; Gatignol, R. Asymptotic Modeling of the Flow of a Binary Gas Mixture in a Microchannel. *AIP Conf. Proc.* **2012**, *1501*, 742–749.
35. Morini, G.L. Viscous Heating. In *Encyclopedia of Microfluidics and Nanofluidics*; Li, D., Ed.; Springer: Boston, MA, USA, 2013; pp. 1–11.
36. Tunc, G.; Bayazitoglu, Y. Heat transfer in microtubes with viscous dissipation. *Int. J. Heat Mass Transf.* **2001**, *44*, 2395–2403. [CrossRef]
37. Aydın, O.; Avcı, M. Heat and fluid flow characteristics of gases in micropipes. *Int. J. Heat Mass Transf.* **2006**, *49*, 1723–1730. [CrossRef]
38. Colin, S. Gas Microflows in the Slip Flow Regime: A Critical Review on Convective Heat Transfer. *J. Heat Transf.* **2011**, *134*, 020908. [CrossRef]
39. Moffat, R.J. Using uncertainty analysis in the planning of an experiment. *ASME Trans. J. Fluids Eng.* **1985**, *107*, 173–178. [CrossRef]
40. Design Institute for Physical Property Research/AIChE, 2009, Sponsored by AIChE DIPPR Project 801—Full Version. Available online: https://dechema.de/ (accessed on 12 November 2021).
41. Zhou, F.; Zhou, W.; Qiu, Q.; Yu, W.; Chu, X. Investigation of fluid flow and heat transfer characteristics of parallel flow double-layer microchannel heat exchanger. *Appl. Therm. Eng.* **2018**, *137*, 616–631. [CrossRef]
42. Zargartalebi, M.; Azaiez, J. Heat transfer analysis of nanofluid based microchannel heat sink. *Int. J. Heat Mass Transf.* **2018**, *127*, 1233–1242. [CrossRef]
43. Kuddusi, L.; Çetegen, E. Prediction of temperature distribution and Nusselt number in rectangular microchannels at wall slip condition for all versions of constant heat flux. *Int. J. Heat Fluid Flow* **2007**, *28*, 777–786. [CrossRef]
44. Hajmohammadi, M.R.; Alipour, P.; Parsa, H. Microfluidic effects on the heat transfer enhancement and optimal design of microchannels heat sinks. *Int. J. Heat Mass Transf.* **2018**, *126*, 808–815. [CrossRef]

45. Demsis, A.; Verma, B.; Prabhu, S.V.; Agrawal, A. Heat transfer coefficient of gas flowing in a circular tube under rarefied condition. *Int. J. Therm. Sci.* **2010**, *49*, 1994–1999. [CrossRef]
46. Cai, C.; Sun, Q.; Boyd, I.D. Gas flows in microchannels and microtubes. *J. Fluid Mech.* **2007**, *589*, 305–314. [CrossRef]
47. Harley, J.C.; Huang, Y.; Bau, H.H.; Zemel, J.N. Gas flow in micro-channels. *J. Fluid. Mech.* **1995**, *284*, 257–274. [CrossRef]
48. Zhu, X.; Liao, Q.; Xin, M.D. Gas Flow in Microchannel of Arbitrary Shape in Slip Flow Regime. *Nanoscale Microscale Thermophys. Eng.* **2006**, *10*, 41–54. [CrossRef]
49. Demsis, A.; Verma, B.; Prabhu, S.V.; Agrawal, A. Experimental determination of heat transfer coefficient in the slip regime and its anomalously low value. *Phys. Rev. E* **2009**, *80*, 016311. [CrossRef]
50. Hadi Najafabadi, H.; Keshavarz Moraveji, M. CFD investigation of local properties of Al2O3/water nanofluid in a converging microchannel under imposed pressure difference. *Adv. Powder Technol.* **2017**, *28*, 763–774. [CrossRef]
51. Dongari, N.; Agrawal, A.; Agrawal, A. Analytical solution of gaseous slip flow in long microchannels. *Int. J. Heat Mass Transf.* **2007**, *50*, 3411–3421. [CrossRef]
52. Sarafraz, M.M.; Arya, A.; Hormozi, F.; Nikkhah, V. On the convective thermal performance of a CPU cooler working with liquid gallium and CuO/water nanofluid: A comparative study. *Appl. Therm. Eng.* **2017**, *112*, 1373–1381. [CrossRef]
53. Sarafraz, M.M.; Arjomandi, M. Demonstration of plausible application of gallium nano-suspension in microchannel solar thermal receiver: Experimental assessment of thermo-hydraulic performance of microchannel. *Int. Commun. Heat Mass Transf.* **2018**, *94*, 39–46. [CrossRef]
54. Nicolas, X.; Chénier, E.; Tchekiken, C.; Lauriat, G. Gas Flows with Heat Transfer in Micro Channels: Clarifications about the Nusselt Number. In Proceedings of the CHT17—ICHMT International Symposium on Advances in Computational Heat Transfer, Napoli, Italy, 28 May 2017.
55. Hooman, K. Entropy generation for microscale forced convection: Effects of different thermal boundary conditions, velocity slip, temperature jump, viscous dissipation, and duct geometry. *Int. Commun. Heat Mass Transf.* **2007**, *34*, 945–957. [CrossRef]